Multiscale image analysis of primary atomization in cryogenic liquid rocket engines

Leonardo Geiger, Nicolas Fdida, Luc-Henry Dorey, Christophe Dumouchel, Jean-Bernard Blaisot, Lucien Vingert, Marie Théron

▶ **To cite this version:**

Leonardo Geiger, Nicolas Fdida, Luc-Henry Dorey, Christophe Dumouchel, Jean-Bernard Blaisot, et al.. Multiscale image analysis of primary atomization in cryogenic liquid rocket engines. ECM 2023, INSA, Apr 2023, Rouen, France. hal-04132952

HAL Id: hal-04132952

https://hal.science/hal-04132952

Submitted on 20 Jun 2023

Multiscale image analysis of primary atomization in cryogenic liquid rocket engines

Leonardo Geiger*[1,2], Nicolas Fdida[1], Luc-Henry Dorey[1], Christophe Dumouchel[2],
Jean-Bernard Blaisot[2], Lucien Vingert[1], and Marie Théron[3]

[1]DMPE, ONERA, Université Paris Saclay, F-91123 Palaiseau, France
[2]CORIA, CNRS, Normandie Université, UNIROUEN, INSA ROUEN, Rouen, France
[3]CNES, Launchers Directorate, Paris, France

Abstract

This paper presents an experimental study of atomization in cryogenic liquid rocket engines. Backlighting images of atomization under reactive subcritical conditions are obtained at ONERA's MASCOTTE test bench. The primary atomization of the liquid oxygen jet assisted by a gaseous methane coaxial flow is studied with a multiscale analysis method capable of measuring characteristic scales of the atomization process. The importance of the optical resolution of the imaging system on the measurement of small liquid ligament sizes is addressed.

Keywords: Atomization, scale distributions, liquid-gas interface, spray combustion, rocket engines.

Introduction

The two-phase coaxial atomization of cryogenic propellants in rocket engine combustion chambers is usually described by global characteristics such as liquid core length and flow shear angle in the primary atomization zone, in addition to droplet number, size and velocity distributions [1–3]. The numerical simulation of atomization inside rocket engine combustion chambers has so far relied on these experimental data [4] for the validation of the models developed. However, more detailed simulations are required to model complex phenomena such as combustion instabilities, which depend on mechanisms such as the primary breakup of the liquid flow. This breakup results from the destabilization and fragmentation of the liquid jet into ligament structures, under the effect of the shear forces from the high-velocity coaxial gas flow, and leads to the production of droplets [5]. From an experimental point of view, very few techniques allow an in-depth description of this primary breakup.

Under reactive conditions such as those encountered in this study, the flows present strong velocity and density gradients that provoke variations in the refractive index of the gaseous medium. This effect, which is magnified close to the flame-front region, is responsible for the high complexity of the obtained images. Moreover, the liquid jet shows deformations and ligament structures of many different sizes (see Figure 1a), making the quantitative analysis of these images challenging. The same difficulties are encountered while designing numerical simulations of these atomization configurations [6].

A multiscale description of primary atomization developed by Dumouchel et al. [7, 8] has shown promising results for the description of atomizing liquid jets. The objective of this study is to develop a multiscale image analysis technique, based on this method, to measure the size of atomizing liquid structures in reactive subcritical conditions such as those encountered inside the combustion chambers of rocket engines burning liquid oxygen (LOx) and methane (CH_4). High-speed backlighting images showing the liquid-gas interface at different optical resolutions are obtained experimentally and analyzed with an image processing technique. The different scales present in such complex systems can be measured leading to the construction of a scale distribution. Characteristic structural scales in the liquid flow, as well as textural scales from ligaments still attached to the liquid jet, can then be identified. This experimental study presents the developed image processing methodology and the multiscale analysis used to measure these scales in the intact liquid system for different operating conditions. The influence of optical and numerical spatial resolution of the images on the accuracy of the measured scales is discussed.

Experimental setup

The MASCOTTE test bench at ONERA Palaiseau allows the study of different physical phenomena involved in the cryogenic combustion of rocket propellants [9]. In the configuration used in this study, the propellants are injected into the combustion chamber by a shear coaxial injector. The liquid oxidizer (LOx) is injected through a circular central tube while the fuel (CH_4) is injected in gaseous phase and at high velocity through an annular gap around the oxidizer central injector. The shear stresses provoked by the strong velocity gradient at the liquid-gas interface are the dominant mechanism in the atomization of the liquid jet.

The chamber pressure achieved by the combustion and acceleration of the propellants is such that the flow regime is subcritical, with a well-defined interface

---

*Corresponding author: leonardo.geiger@onera.fr

separating the two phases of the flow. The oxygen flow is considered subcritical when the temperature and pressure of the propellants are less than their critical values ($P < P_c$, $T < T_c$). The mixture ratio M, defined as the ratio between the oxidizer and fuel mass flow rates, is near stoichiometry ($M_{st} = 4$ for LOx-CH_4 combustion) but slightly fuel-rich, with a value representative of rocket engine combustion chambers ($M \approx 3{,}5$). Three target operating points were defined with constant mixture ratio and liquid injection velocity, and varying chamber pressure and gas injection velocity. The main parameters are the chamber pressure P, the mixture ratio M, the momentum flux ratio J, defined as the ratio between the gas and liquid momentum fluxes, the injection liquid Reynolds number Re_l based on the diameter of the oxygen injector D_{LOx}, and the relative Weber number We_R, defined as the ratio of aerodynamic forces to surface tension, or

$$We_R = \frac{\rho_{CH_4}(V_{CH_4} - V_{LOx})^2 D_{LOx}}{\sigma}$$

These parameters are grouped in Table 1. The momentum flux ratio is adimensionalized by a reference value J_{ref} equal to the momentum flux ratio of operating condition B. These operating conditions were chosen to highlight the influence of the parameters most strongly to the atomization process, namely the pressure and the momentum flux ratio, on the liquid flow morphology.

O.C.	P (bar)	J/J_{ref}	M	Re_l	We_R
A	7	1.30	~ 3.5	$\sim 7\text{x}10^4$	$\sim 3\text{x}10^4$
B	10	1			
C	15	0.75			

Table 1: Tested operating conditions.

The combustion chamber is equipped with two optical accesses allowing the use of non-intrusive optical diagnostics. In this study, the fragmentation of the liquid jet is visualized through a backlighting imaging technique while the flame front can be simultaneously visualized through imaging of the OH* radical chemiluminescence.

The high-speed backlighting images showing the liquid flow are obtained with a Phantom 711 camera from Vision Research whose CMOS sensor contains 1280x800 squared pixels of 20 μm side length. The camera is equipped with a Nikon lens of 200 mm focal length. The light source is a Cavilux Smart 400 W laser emitting a red incoherent light pulse at a wavelength of 640 ± 10 nm. The pulse duration is set at 30-40 ns to freeze the flow appropriately. A narrow band filter allows the light source to reach the sensor but blocks light from the flame emission. The OH* chemiluminescence is captured using a UV imaging system composed of a high-speed VEO710 Phantom camera and a LaVision HSIRO intensifier. The camera is equipped with a CERCO UV lens of 100 mm focal length and a filter corresponding to the OH* spectral signature of 310 nm ± 10 nm. The exposure time of the intensifier was set to 5 μs.

Figure 1a shows a snapshot of the backlighting images obtained for operating condition B showing the liquid oxygen flow in dark against a light gaseous background. Time-averaged backlighting and Abel-transformed OH* chemiluminescence images, showing respectively the liquid oxygen and the flame, are superimposed in Figure 1b. This composite image shows the relative position of the flame and the liquid jet. It shows that, near the injection plane, the flame is located very close to the dense liquid jet, in the mixing layer between the liquid and gaseous flows, as the small droplets produced in this primary atomization zone are burned very quickly after being produced. As the flow develops in the downstream direction, larger liquid ligaments are produced and accelerated away from the dense liquid core by the high-speed gas flow. The droplets produced by these larger ligaments are more distant from the liquid core and thus the flame front is also found to spread from the dense liquid jet. This results in the flame opening angle in the composite image after around three LOX diameters in the downstream direction. A very similar behavior is observed for the other operating conditions tested.

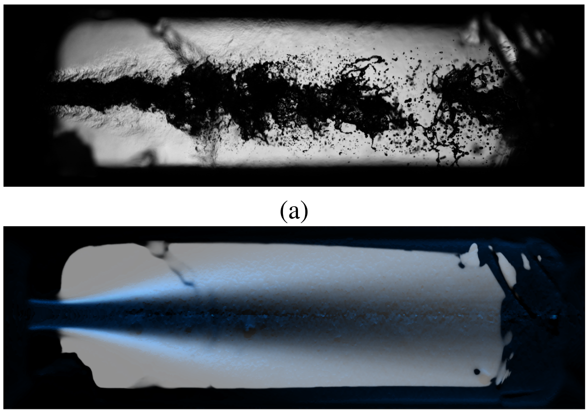
(a)

(b)

Figure 1: Experimental images for O.C. B: (a) backlighting snapshot and (b) time-averaged backlighting and Abel-transformed OH* chemiluminescence composite image.

Multiscale analysis

The image analysis method developed in this study analyses the liquid system through a set of morphologic descriptors called the Minkowski Functionals (MFs). In two dimensions, the MFs measure the surface area S, the interface length L and the length-integrated-curvature H of the system. The system is characterized by its MFs as well as those of all systems parallel to it in the liquid phase. These parallel systems are obtained by erosion operations at all possible scales d for which the distance between the system interface and that of one of its parallel systems is equal to $d/2$.

In practice, measurements are made on binary images showing the liquid system as black pixels against a white background, as seen in Figures 2a and 4b. The segmentation of the raw experimental images is achieved by a local Phansalkar threshold method [10]. The erosions at different scales d are performed through the Euclidean Distance Map (EDM) of the binary system. The EDM transformation assigns to each black (liquid) pixel a gray level equal to its shortest distance to the interface. A cumulative count of the pixels based on the assigned gray levels allows to measure the surface area of the parallel liquid systems as a function of the distance to the interface. The MFs are determined through the construction of another set of functions related to the MFs [8]: the cumulative scale distribution $E_2(d)$, defined as:

$$E_2(d) = S(0)–S(d) \tag{1}$$

with $S(0)$ and $S(d)$ being the surface areas of the original liquid system and of its parallel system at a distance $d/2$ to the interface, the scale distribution $e_2(d)$ defined as the derivative of $E_2(d)$ with respect to d:

$$e_2(d) = E_2(d)_{,d} \tag{2}$$

and the derivative of the scale distribution $e_2'(d)$:

$$e_2'(d) = e_2(d)_{,d} \tag{3}$$

Once $E_2(d)$ is measured with the help of the EDM transformation, the scale distribution $e_2(d)$ and its derivative $e_2'(d)$ are obtained through successive derivations of $E_2(d)$.

It has been shown [7] that the scale distribution $e_2(d)$ is proportional to the interface length of the parallel system obtained from erosion at scale d. One of the interests of the $e_2(d)$ function is that its derivative with respect to the scale d exhibits discontinuities at scales corresponding to throughs and swellings of the liquid system [8]. The next section illustrates this for a synthetic system.

Synthetic image analysis

Figure 2a shows a synthetic system made of two ligaments with sinusoidal surface perturbations. Their lengths are equal to one disturbance wavelength and their undisturbed diameter is 40 pixels. The perturbation wavelength is 800 pixels and the perturbation amplitude is 20 and 35 pixels, respectively. The characteristic scales of this type of jet are its maximum and minimum diameters, i.e., 60 and 75 pixels and 5 and 20 pixels, respectively. Two measurements are made using images of different spatial resolutions, one with the reference resolution R (corresponding to the given ligament dimensions) and another with a resolution four times superior, 4R. The resulting $-e_2'(d)$ measured with two different resolutions is shown in Figure 2b.

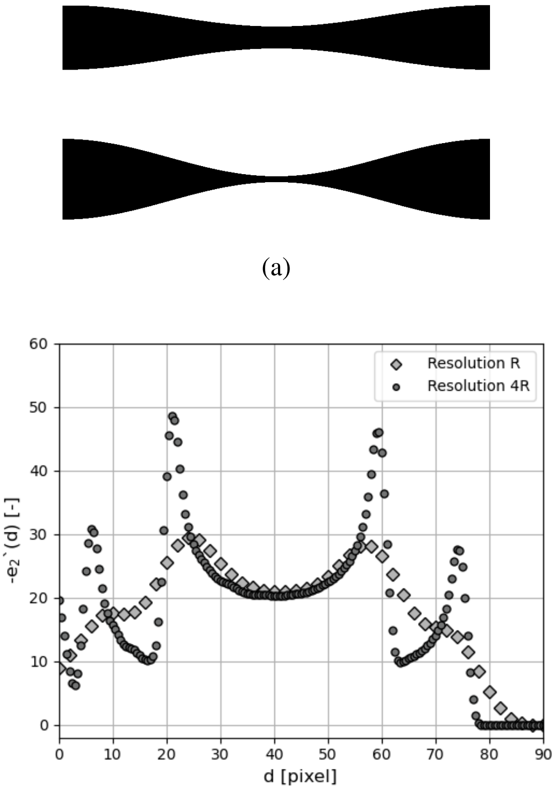

Figure 2: Multiscale analysis of a synthetic system with two spatial resolutions. (a) Synthetic image and (b) resulting $-{e_2}'(d)$.

The measurements report peaks that are the marks of the theoretical discontinuities expected at 5, 20, 60 and 75 pixels. The $-e_2'(d)$ plot of the image at resolution R shows four peaks representing the four characteristic scales of the system. However, these peaks are not very well marked, and their positions show an error of ±5 pixels when compared to the expected values. On the other hand, the measurement on the higher-resolution image shows peaks with better-marked positions and an error of ±1 pixel.

These results show that an increase in spatial resolution improves the accuracy of the measurement of the characteristic scales of the system. They also show an error in the very-small-scale zone (up to $d = 5$ pixels) attributed to pixelization on the images. Indeed, as shown by Dumouchel et al. [8] for ligamentary systems as the one examined in Figure 2, $e_2'(0)$ must be equal to 0. These observations will prove useful for interpreting the experimental results in the next section.

Image interpolation

The fact that measurements presented in Figure 2b show values that differ from zero at small scales is due to the pixelization and therefore to the image resolution. This means that, if the image resolution is increased, the pixel size decreases and the physical size of the error range decreases. The problem is thus limited to smaller physical scales. To numerically increase the resolution of the images, a sub-pixel analysis is proposed. A bilinear image interpolation procedure is applied to increase the number of pixels in the experimental images. For example, a *Hx* interpolation transforms an *NxN* raw image into a *HNxHN* interpolated image. To be coherent with the theory, the measured $-e_2'(d)$ should show a peak in the small-scale zone. If this peak is found, it will be considered as a mark of the size of the small liquid ligaments. Some examples are shown in the next section.

Results

One of the goals of this study is to assess the influence of spatial resolution on the measurement of small textural elements on the experimental liquid-gas interface. To do so, backlighting images were obtained with two spatial resolutions: 60 μm/pixel and 20 μm/pixel. Figure 3a and 3b show respectively a snapshot of each resolution. In both cases, the visualized field corresponds to a near-injector flow region of equal length.

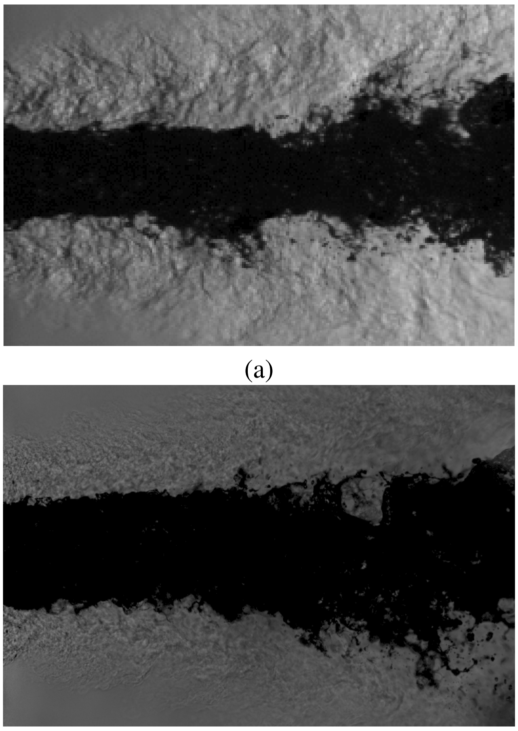
(a)

(b)

Figure 3: Near-injector field backlighting snapshots of O.C. A with two optical resolutions: (a) 60 μm/pixel and (b) 20 μm/pixel.

Figure 4 shows the result of the segmentation and interpolation of one experimental snapshot of operating condition A with 60 μm/pix resolution. Figure 5 shows the result of the image interpolation technique on an individual liquid ligament highlighted in Figure 4.

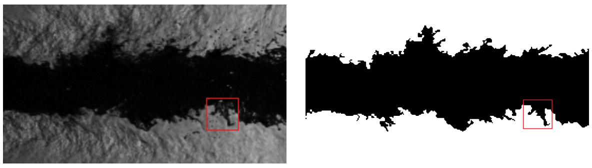
(a) (b)

Figure 4: Image processing step: (a) initial raw backlighting snapshot and (b) resulting binary image.

(a) (b) (c)

Figure 5: Effect of image interpolation on an individual liquid structure highlighted in Figure 4: (a) raw, (b) binary and (c) 12x interpolated binary images.

Once the images are segmented, the multiscale image analysis technique can finally be applied. Figures 6a and 6b show the time-averaged measured $-e_2'(d)$ in the small- and large-scale regions respectively with 60 μm/pix resolution images. Scales are adimenzionalized by a reference scale d_{ref} equal to the diameter of the oxidizer injector. Two different levels of pixel interpolation are compared: 3x and 12x (see Figure 5). As mentioned previously, the analysis of ligamentary structures imposes $e_2'(0) = 0$. Figure 6a shows that, in the small-scale region, the interpolation provides a better measurement, with the exception of the first three points where the pixelization error still occurs. Indeed, the 12x interpolated images curve shows a peak suggesting the capture of the smallest scales in the image and a decrease towards zero (the expected qualitative result in the vicinity of $d = 0$ is shown by the dashed line). The captured peak, located at $d/d_{ref} = 0.023$, represents the smallest scales captured by the method. As a comparison, the smaller liquid structure shown in Figure 5 measures approximately $0.027d_{ref}$.

Figure 6b, in turn, shows the large scales measured. It can be seen that the highest interpolation does not result in a better measurement since the two curves almost superimpose. The curves show the distribution of structural scales of the liquid jet, with a peak located at $d/d_{ref} = 0.87$. The curve is fairly symmetrical (it shows a slight positive skew). This means that most of the measured scales are smaller than the reference scale, which indicates that, in the examined position, the jet diameter is smaller than that of the injector, on average.

The small-scale measurements on images with 60 μm/pix and 12x interpolation allowed to capture the expected small-scale peak. The same approach is used to compare the different optical resolutions tested in this study (20 and 60 μm/pix). Figure 7 compares

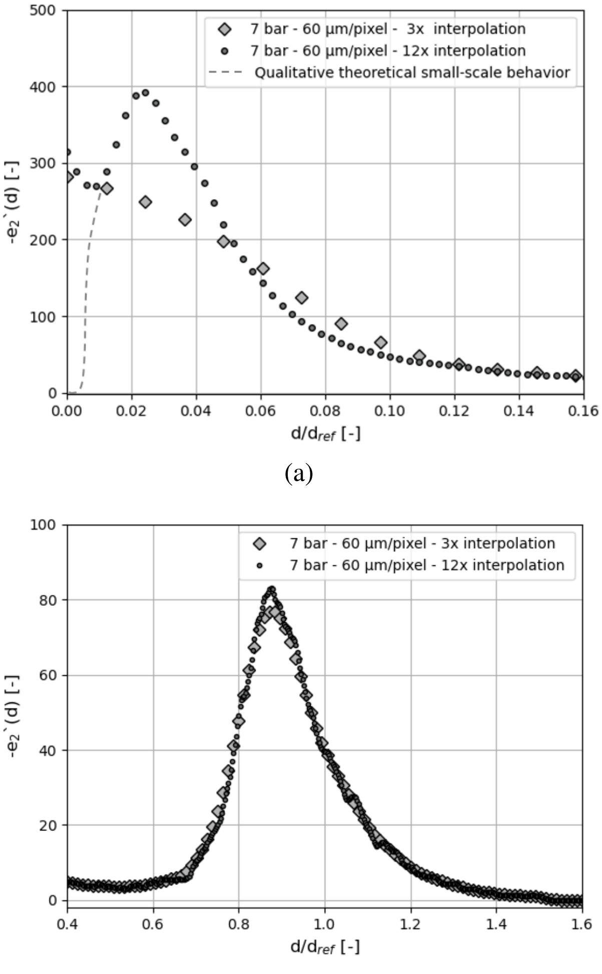

(a)

(b)

Figure 6: Comparison of $-e'_2(d)$ measured on images of 60 μm/pix optical resolution with 3x or 12x interpolation: (a) small and (b) large scales.

the time-averaged small-scale $-e'_2(d)$ measurements of O.C. B and C with both optical resolutions in the small-scale range. The increase in optical resolution has the same overall effect on both operating points: results for both low- and high-resolution images (with appropriate numerical interpolations of 12x and 8x, respectively) show a peak in the small-scale region. The position of the peaks appears to only depend on the optical resolution of the images. For the optical resolution of 60 μm/pix, the peaks are found at around $d/d_{ref} = 0.023$, as in Figure 6a for O.C. A. Meanwhile, for the optical resolution of 20 μm/pix, the position of the peaks is around $d/d_{ref} = 0.010$. This shows that, with an increase in the optical resolution of the raw images, smaller liquid structures are visualized and measured. Also, the value of $-e'_2(d)$ at the peaks is higher (around twice as high) for the higher-resolution images compared to the lower-resolution ones. This indicates that a higher quantity of liquid structures of this size can be found in the higher-resolution images.

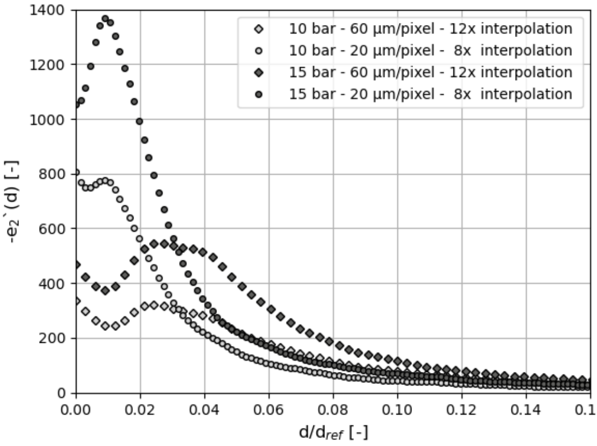

Figure 7: Effect of optical resolution on the small-scale $-e'_2(d)$ measured on images of 60 μm/pix or 20 μm/pix for two operating points.

Finally, Figure 8 compares $-e'_2(d)$ for all three operating conditions, measured on the high-resolution images of 20 μm/pix with an 8x image interpolation. The resulting time-averaged $-e'_2(d)$ show once again a peak in the small-scale zone, associated with the smaller liquid structures. As seen in Figure 7, the position of these peaks is the same for all operating points. Differences are found, however, in the value of $-e'_2(d)$ at each of the peaks. This value indicates the quantity of liquid structures of this smallest size. O.C. C shows the highest value at the peak, followed by O.C. A, while O.C. B shows the lowest peak. Another difference is found in the relative height of the curves between $d/d_{ref} = 0.01$ and $d/d_{ref} = 0.16$, as in Figure 7 for O.C. B and C. Results for O.C. B show lower values of $-e'_2(d)$ (thus a lower quantity of liquid structures) than O.C. A and C through all of the shown small-scale interval. Meanwhile, an interesting behavior is found comparing O.C. A and C. The latter shows a higher value at the peak, and this behavior switches at around $d/d_{ref} = 0.025$. From this scale until $d/d_{ref} = 0.16$, the curve for O.C. A is higher, meaning that the associated images show more liquid structures of these sizes.

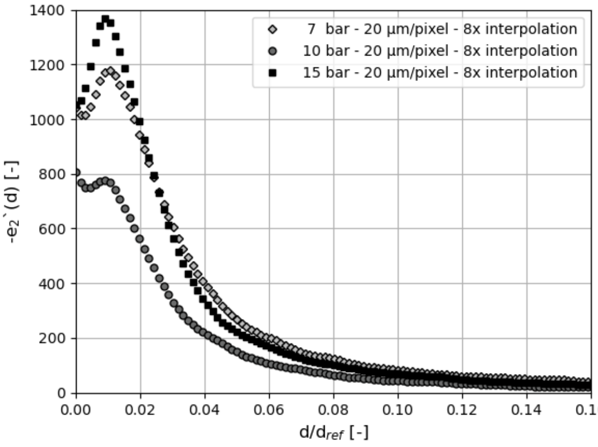

Figure 8: Comparison of small-scale $-e'_2(d)$ on 20 μm/pix resolution images for all three operating conditions.

These results show an improvement in the measurement of the size of small-scale liquid structures in the flow. The increase in optical resolution showed an improvement in the measurement, allowing to capture smaller liquid structures. The differences observed between the different operating points, however, require further investigation. Indeed, the individual influence of the atomization parameters such as chamber pressure and momentum flux ratio on the size and quantity of liquid ligaments has not yet been clarified.

Conclusion

In this paper a multiscale image analysis technique is presented and applied to backlighting images of an atomizing liquid oxygen jet under subcritical reactive conditions with a coaxial methane gas flow. The effect of optical and numerical image resolution on the measurement of the small-scale structures produced at the interface of the liquid-gas system is studied. The measurements are applied on three different operating conditions representative of subcritical rocket engine combustion chamber conditions.

It is shown that a numerical image interpolation enhances the accuracy of the small-scale measurements. This image interpolation is not, however, capable of recovering information that was lost due to an insufficient optical resolution in the experimental imaging system (such as very small liquid structures). An increase of optical resolution from 60 μm/pix to 20 μm/pix corresponds to a reduction of the scale representing the size of the smallest liquid structures measured by the multiscale method. It also corresponds to a strong increase in the value of $-e_2'(d)$ in the small-scale range, which indicates an increase in the presence of small structures in the images. The fact that, for both optical resolutions, the measured size of the smallest structures is close to the pixel size in the corresponding original images may indicate that an even higher resolution could be required to capture all of the smallest liquid ligaments in the flow. Very high-resolution images of the flow should be measured using the same methodology to assess this hypothesis.

Finally, the measurement of the size of the smallest liquid structures in these flow conditions represents a significant progress towards the understanding of the initial jet breakup leading to the production of new liquid drops in the flow, which may or may not breakup into even smaller droplets, depending on their size and velocity. Also, the knowledge of the size of the small liquid ligaments is very important in the design of numerical simulations which, due to computational costs, must try to optimize the grid resolution to capture the small ligaments in the flow using a mesh that is as coarse as possible. The methodology presented here allows to obtain measurements that can be used to validate the results of numerical simulations through comparisons between the simulated ligaments and those seen in the experimental images. It may also be used to compare images of atomizing jets with and without acoustic excitation in order to quantify the interaction between acoustics and atomization in the study of high-frequency combustion instability mechanisms.

References

[1] B. Yang, F. Cuoco, and M. Oschwald, Atomization and flames in LOX/H2- and LOX/CH4-spray combustion, *Journal of Propulsion and Power* **23**, 763 (2007).

[2] S. Boulal, N. Fdida, L. Matuszewski, L. Vingert, and M. Martin-Benito, Flame dynamics of a subscale rocket combustor operating with gaseous methane and gaseous, subcritical or transcritical oxygen, *Combustion and Flame* **242**, 112 (2022).

[3] N. Fdida, L. Vingert, A. Ristori, and Y. Le Sant, Droplet size and velocity measurements in a cryogenic jet flame of a rocket-type combustor using high-speed imaging, *Atomization and Sprays* **26** (2016).

[4] C. Le Touze, L.-H. Dorey, N. Rutard, and A. Murrone, A compressible two-phase flow framework for large eddy simulations of liquid-propellant rocket engines, *Applied Mathematical Modelling* **84**, 265 (2020).

[5] P. Marmottant and E. Villermaux, On spray formation, *Journal of Fluid Mechanics* **498**, 73 (2004).

[6] P. Gaillard, C. Le Touze, L. Matuszewski, and A. Murrone, Numerical simulation of cryogenic injection in rocket engine combustion chambers, *Aerospace Lab* 16 (2016).

[7] C. Dumouchel, J.-B. Blaisot, F. Abuzahra, A. Sou, G. Godard, and S. Idlahcen, Analysis of a textural atomization process, *Experiments in Fluids* **60**, 1 (2019).

[8] C. Dumouchel, F. Thiesset, and T. Ménard, Morphology of contorted fluid structures, *International Journal of Multiphase Flow* **152**, 104 (2022).

[9] M. Habiballah, M. Orain, F. Grisch, L. Vingert, and P. Gicquel, Experimental studies of high-pressure cryogenic flames on the MASCOTTE facility, *Combustion Science and Technology* **178**, 101 (2006).

[10] N. Phansalkar, S. More, A. Sabale, and M. Joshi, in *2011 International Conference on Communications and Signal Processing* (2011), 218–220.